Identification of a unique pyridinic FeN_4C_x electrocatalyst for N_2 reduction : tailoring the coordination and carbon topologies

Identification of a unique pyridinic FeN_4C_x electrocatalyst for N_2 reduction: tailoring the coordination and carbon topologies

Parisa Nematollahi[*a], Erik C. Neyts[a]

[a] Research Group Plasmant, NANOlab Center of Excellence, Department of Chemistry, University of Antwerp, Universiteitsplein 1, 2610 Antwerp, Belgium

* Corresponding author. **Phone:** (+32) 32652346. **E-mail**: parisa.nematollahi@uantwerpen.be

Abstract

Although the heterogeneity of pyrolyzed Fe-N-C materials is known and reported previously, the atomic structure of the active sites and their detailed reaction mechanisms are still unknown. Here, we identified two pyridinic Fe-N_4-like centers with different local C coordinates i.e., FeN_4C_8 and FeN_4C_{10}, and studied their electrocatalytic activity for nitrogen reduction reaction (NRR) based on Density Functional Theory (DFT) calculations. We also discovered the influence of adsorption of NH_2 as a functional ligand on catalyst performance on the NRR. We confirmed that the NRR selectivity of the studied catalysts is essentially governed either by the local C coordination or by the dynamic structure associated with the Fe^{II}/Fe^{III}. Our investigations indicate that the proposed traditional pyridinic FeN_4C_{10} has higher catalytic activity and selectivity for NRR than the robust FeN_4C_8 catalyst while it may have an outstanding activity for promoting other (electro)catalytic reactions.

Keywords: Nitrogen reduction, Fe-N-C materials, ligand effect, DFT

Introduction

The slow kinetics of the electrochemical nitrogen reduction reaction (NRR) is an important issue that contributes significantly to the total cost [1]. Therefore, various investigations have focused on the development of effective catalysts with low cost and high efficiency [2-4]. In the last decades, single-metal atom catalysts (SACs) have emerged and are widely used for diverse catalytic reactions due to their high catalytic activity and selectivity [5-8]. One of the most promising classes of catalysts is transition metal (TM) doped pyridinic or porphyrinic N_4 active-sited embedded carbon catalysts [8-9]. FeN_4/C catalyst represents outstanding electrocatalytic activity for oxygen reduction reaction (ORR) reported in previous investigations [10-12].

In 2009, Lefèvre et al. [13] produced microporous carbon-supported Fe-based catalysts for ORR. They believed that the active sites contain Fe cations coordinated by pyridinic nitrogen functionalities in between the graphitic sheets within the micropores. The FeN_4 motif is distinguished as the active site in which the Fe atom binds strongly with the surrounding N atoms stabilizing the Fe atom [14]. Against the bulk structure, the FeN_4/C nanosheet is more active toward electrocatalytic reactions with higher selectivity. This can be due to the excellent separation between the Fe atoms distributed all over the surface. Moreover, two sides of the pure FeN_4 sites are uncovered. This makes the pure FeN_4 sites able to interact with the available reactants and intermediates in the environment, even the ions or molecules which are not a part of the NRR process, during the catalytic process. In addition, it is possible that only one side of the Fe active center binds with a molecule as a functional ligand and leaves the other side of the catalyst available for NRR. This will certainly modify the electronic states of the FeN_4 center and changes the total catalytic activity of the catalyst. The effects of the ligand on the ORR and NRR activity of TMN_4/C catalysts have been proven by previous experimental and theoretical investigations [15-18]. For instance, Wang et al. investigated the adsorption of a series of inorganic molecules and ions onto Fe-N_x/C catalysts and its effect on the ORR activity. They revealed that the ORR activity is slightly suppressed by halide ions, while it is significantly suppressed by

sulfur-containing species (e.g., SCN^-, SO_2, and H_2S) [19].

In addition to the ligand effect, it is known that the topology of the local C atoms surrounding FeN_4 active centers has a great effect on its electrocatalytic activity. In a recent combined DFT and experimental investigation, Jia et al. [20] showed that the catalytic activity of FeN_4C_8 in the presence of a fifth ligand is governed by its dynamic structure associated with the $Fe^{II/III}$ redox transition rather than the static structure of the base sites. Fe plays a crucial role in nitrogenase (Fe-protein and MoFe-protein) for biological N_2 fixation and is also widely used in the Haber-Bosch process for ammonia synthesis [21]. Recent reports also indicated that the Fe-N-C materials can be considered as a promising catalyst for NRR at room temperature [22-23]. For instance, Li et al. [17] find that FeN_3-embedded graphene can be considered as a robust catalyst for the NRR at ambient temperatures, especially with high-spin polarization of active FeN_3 centers. Wang et al. [24] studied the precise construction of efficient and stable NRR electrocatalysts. They designed and implemented a Fe−N/C−carbon nanotube (CNT) catalyst with built-in Fe−N_3 active sites by carbonizing Fe-doped zeolitic-imidazolate framework (ZIF) deposited on the surface of CNTs. The porous structure, large active surface area, positively charged surface, weak ferromagnetism, and strong nitrogen chemisorption are all favorable for NRR electrocatalysis. The electrocatalyst exhibits a high NH_3 yield and a faraday efficiency (FE) of 9.28% at −0.2 V in 0.1 M KOH. They confirmed that the introduction of Fe atoms into N/C-CNTs significantly increases the NRR performance.

Although several works so far have been reported on NRR, the effects of different ligands along with the local C coordination on N_2 fixation have not been studied extensively yet. Therefore, to improve the NRR activity of a catalyst, finding a good combination of the ligand and active site is necessary. In this work, we characterize the active sites in FeN_4/C catalysts by comparing density functional theory (DFT) simulations and ^{57}Fe Mössbauer spectroscopy data to study the influences of local C topology and ligand on the electrocatalytic NRR over FeN_4/C catalyst. We propose two pyridinic FeN_4/C catalysts i.e., FeN_4C_8 and FeN_4C_{10}, and study the electrocatalytic NRR with and

without the presence of an NH_2 ligand. This work indicates that the pyridinic FeN_4C_8 is more selective for NRR while using the functional ligand can significantly reduce the electrocatalytic activity of the catalyst. Therefore, our results may serve as a further guide to a broader combination of functional ligands and metal centers for NRR and other related catalytic reactions.

Computational details

All DFT calculations are spin-polarized using the Vienna ab initio simulation package (VASP) [25-27]. The exchange and correlation energies were described by the generalized gradient approximation (GGA) in the form proposed by Perdew-Burke-Ernzerhof (PBE) [28]. The ion-electron interactions are described by the projected augmented wave (PAW) method [29]. Convergence of the plane-wave cutoff energies was checked and cutoff energy of 400 eV is chosen and employed in all calculations. The convergence criterion for the residual force and energy in structural relaxations was set to 0.01 eV/Å and 10^{-6} eV, respectively. Partial occupancies are addressed using Gaussian smearing with a smearing width of 0.01 eV. The zero-damping Grimme approximation, DFT + D_2, is used to compute the weak dispersion interactions [30]. Two different FeN_4C models are simulated with different local C topologies, i.e., FeN_4C_8 (complex A) and FeN_4C_{10} (complex B), representing the most common models found in the literature [20, 31-34]. All models are constructed using VESTA [35] by modifying a graphene layer. A unit cell of 4×3 and 4×2 is used for complexes A and B, respectively. For structure relaxations, the first Brillouin zone of such a slab is sampled with the Monkhorst−Pack mesh of 5 × 5 × 1 k-points. To get more accurate electronic property computations, denser 15 × 15 × 1 k-point grids were employed [36]. To avoid interactions between two neighboring 2D FeN_4/C sheets, a minimum vacuum space of 15 Å was set between the two layers. Atomic charges and charge transfer were calculated from the Bader charge scheme [37]. An optimized N_2 molecule and a bulk Fe are used as a reference for calculating the adsorption energy of atomic nitrogen on the surface and Fe atom into the N_4 vacancies, respectively. For the Fe atom, the pseudopotential that treats 3s and 3p states as valence states is used for all calculations.

The NRR performance is calculated by the Gibbs free energy change (ΔG) of the elementary reaction using the computational hydrogen electrode (CHE) model proposed by Nørskov et al. [38-39]. According to the CHE model, the change in the free energy for each reaction step can be expressed by:

$$\Delta G = \Delta E + \Delta ZPE - T\Delta S + \Delta G_{pH} + \Delta G_U \quad (1)$$

where ΔE is the calculated total energy, ΔZPE is the change in the zero-point energy (ZPE), T is the room temperature (298.15 K), and ΔS is the changes in standard vibrational entropy. Both ΔZPE and ΔS values are obtained from vibrational frequency calculations using the VASPKIT code [40]. To reduce the computational complexity, only the vibrational frequency of adsorbates is calculated because the translational and rotational degrees of freedom of the adsorbate effectively convert into vibrational modes (frustrated translations and rotations) and the surface atoms are fixed, assuming that the vibrations of the solid surface are negligible. Notably, for the gas phase molecules, the entropy term can be obtained by the sum of the translational, rotational, and vibrational contributions. ΔG_{pH} refers to the free energy correction of the pH with the formula expressed as $\Delta G_{pH} = k_B T \times pH \times \ln 10$, where k_B is the Boltzmann constant and the value of pH is set to be 0 for this work. ΔG_U is the free energy contribution related to the applied electrode potential (U) versus standard hydrogen electrode (SHE), i.e., $\Delta G_U = -neU$, where n is the number of H+/e^- pairs transferred in NRR and e is the unit charge. U is the applied electrode potential concerning the SHE. The limiting potential (U_{lim}) is equal to the $-\Delta G_{max}/e^-$, where ΔG_{max} is the step that releases the maximum free energy among six steps, that is, the thermodynamic potential determining step (PDS). Theoretical overpotential (η) is adopted as a measure for the whole ORR rate and is then determined as $\eta = U_{equ} - U_{lim}$, where U_{equ} is the equilibrium potential of NRR reaction, which is -0.16 V vs. SHE [41-42].

Results and discussions

Stability of the FeN_4C catalyst

To comprehensively and accurately evaluate the performance of FeN_4C_x catalysts, it is essential to study their stability. Here, the adsorption energy is utilized to describe the stability of either Fe atom

doped into the N_4 vacancy or adsorbed species on the catalyst, and it is defined as follows:

$$E_b = E_{FeN4Cx} - (E_{Fe} + E_{N4Cx}) \quad (2)$$

where the E_{FeN4Cx}, E_{Fe}, and E_{N4Cx} are the total energies of the optimized FeN_4C_x surface, isolated Fe atom, and optimized defective N_4Cx surface, respectively. The more negative the E_b value means the better structural stability. Pristine FeN_4C_x catalyst with a D_{4h} symmetry has a completely planar structure in which all the six electrons of the Fe atom can be associated with the N atoms (see complexes A and B in Figure 1). The Fe oxidation state in these structures is Fe^{II} as reported by Rovira et al. [34] which binds strongly into the N_4 cavities of FeN_4C_8 (E_b= -4.52 eV) and FeN_4C_{10} (E_b= -7.42 eV). The calculated cohesive energy of Fe is -5.74 eV [43]. One can see that the binding energy of complex B is more negative than the bulk Fe cohesive energy, indicating that the stability of complex B is even better than that of the bulk Fe surfaces [44]. The binding energy of complex A is close to the Fe bulk cohesive energy, and this catalyst is synthesized and reported in previous investigations [45-51]. Therefore, we consider it as a stable structure for catalyzing the electrochemical NRR. To gain an insight into the electronic properties of the pure catalysts, we calculated the densities of states (DOS) of a single Fe atom embedded in the N_4C_8 and N_4C_{10} systems as presented in Figure S1. One can see that the spin-up and spin-down states of the Fe-3d band are not symmetric in both complexes which are due to the presence of four N atoms.

In the presence of the fifth ligand, here NH_2^-, the iron oxidation number changes to Fe^{III} [34] with the binding energy of E_b= -2.26 eV and E_b= -0.56 eV for complexes C and D, respectively. The computed Fe−N bond lengths (d_{Fe-N}) of the optimized complexes A, B, C, and D are in the range of 1.85−1.91 Å (see Table S2), in good agreement with previous studies [20, 52-53], showing that by adding the ligand, the Fe−N bond increases for about 0.03 eV.

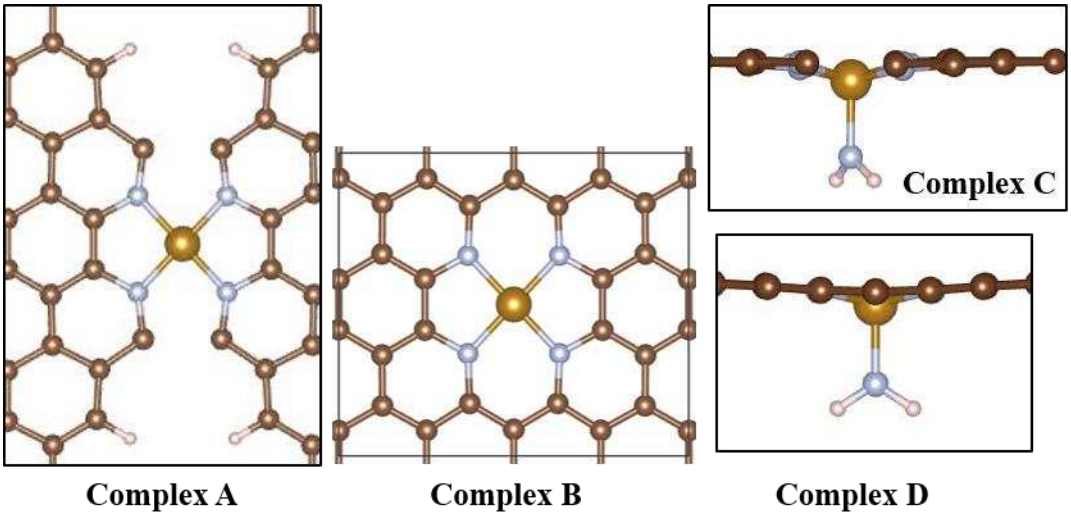

Figure 1. Proposed pristine FeN_4C_8 (complex A) and FeN_4C_{10} (complex B) along with the corresponding NH_2 coordinated structures, $FeN_4C_8@NH_2$ (complex C) and $FeN_4C_{10}@NH_2$ (complex D). In complexes C and D, NH_2 is considered as a fifth ligand. Color code: brown, C; blue, N; orange, Fe; white, H

Adsorption of N_2

The initial configuration of the adsorbed $*N_2$ on the FeN_4 site would change the NRR reaction pathway as shown in Figure 2. Thus, due to the stable triple N≡N bond [42, 54-56], the activation of $*N_2$ on the catalyst surface plays an important role in the NRR process. Therefore, we firstly investigated the adsorption behavior of N_2 on the studied surfaces by calculating the adsorption energy (E_{ads}) defined as $E_{ads} = E_{complex} - E_{adsorbate} - E_{surface}$ where $E_{complex}$, $E_{adsorbate}$, and $E_{surface}$ refer to the total energy of optimized FeN_4C_x catalyst with adsorbate, the individual adsorbate, and the pure FeN_4C_x catalyst, respectively. Screening the adsorption energy of $*N_2$ on complexes A and B (Figure 2a, b, c, and d) and complexes C and D (Figure 2e, f, g, and h) we found that the side-on adsorption is not favored on any of the catalysts except on complex A with a highly E_{ads} of -2.17 eV (see Table S1). According to Figure 3a, the negative adsorption energies suggest that the adsorption of dinitrogen is thermodynamically favorable on the catalyst. However, the end-on orientation dominates the side-on orientation and is thermodynamically more feasible (see Figure 3b).

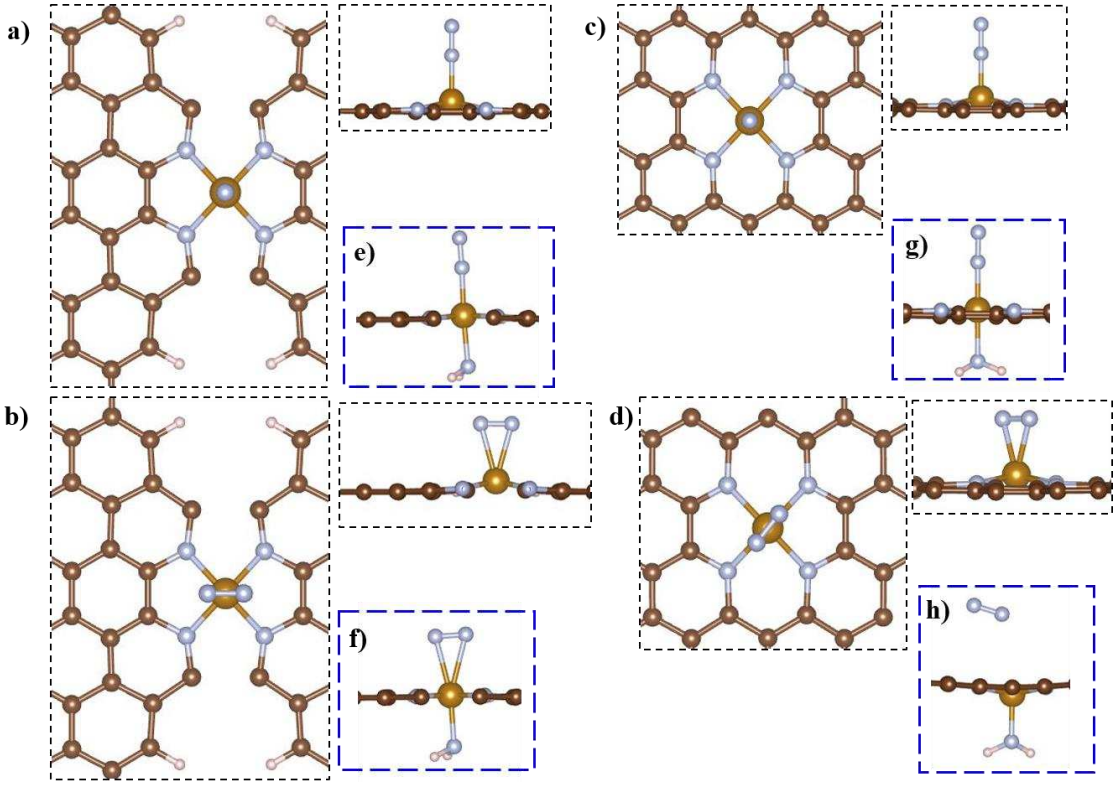

Figure 2. Optimized configurations of end-on and side-on N_2 adsorption on complex A (Figures 2a and 2b), complex B (Figures 2c, and 2d), complex C (Figures 2e and 2f), and complex D (Figures 2g and 2h). Color code: brown, C; blue, N; orange, Fe; and white, H

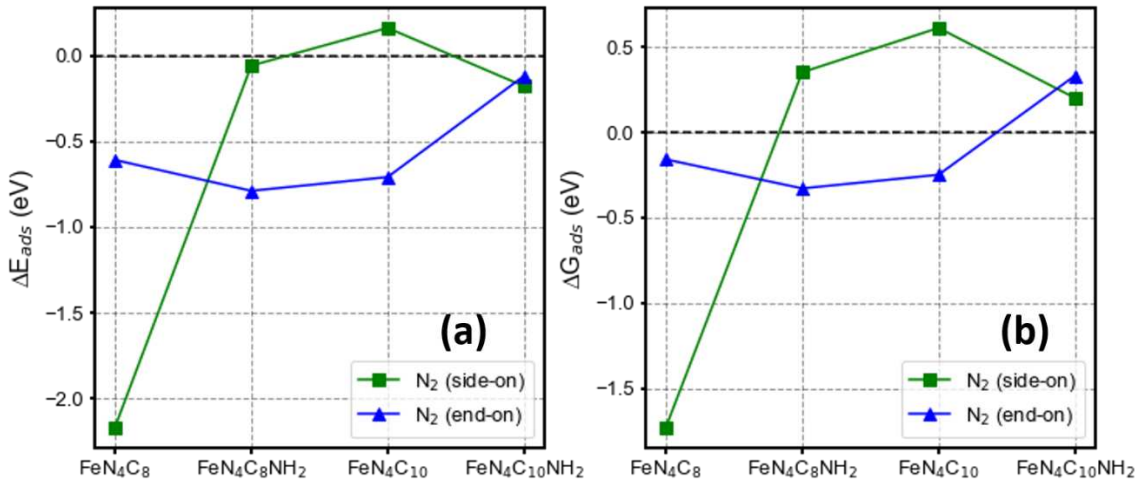

Figure 3. Adsorption energy (a) and the free energy of adsorption (b) for N_2 on complexes A, B, C, and D.

The interaction between $*N_2$ and the Fe active site is dominated by electron acceptance and donation. Fe atom has unoccupied and occupied d-orbitals that either accepts electrons via σ-donation or donate electrons via π back-donation. The π back-donation increases the occupation of the antibonding π^* orbitals of N_2, weakening the triple bond and consequently activating the adsorbed $*N_2$

species [57]. According to the obtained adsorption energies of *N_2 reported in Table S1, the strong interaction between Fe sites and *N_2 leads to more electron transfer to the anti-bonding orbital of *N_2 ($1\pi^*$) which consequently increases the energy of the *N_2@FeN_4/C catalyst and thus decreases the affinity of the catalyst to *N_2.

The thermodynamic feasibility of N_2 adsorption on FeN_4 catalysts is captured through a lower value of change in free energy of N_2 adsorption (ΔG_{N2}). According to Sabatier's principle [58-61], we considered an optimum range of 0.2 to -0.5 eV for the ΔG_{N2} because the adsorption of N_2 should be optimum to obtain high NRR activity (see Figure 4). As shown in Figure 4, the end-on N_2 adsorbed on complexes A, B, and C and the side-on N_2 adsorbed on complex D are placed in this specified range, therefore, these complexes can act as potential candidates for NRR. However, to confirm this, the NRR on the rest of the catalysts outside the optimum range is also studied and reported in the Supporting Information.

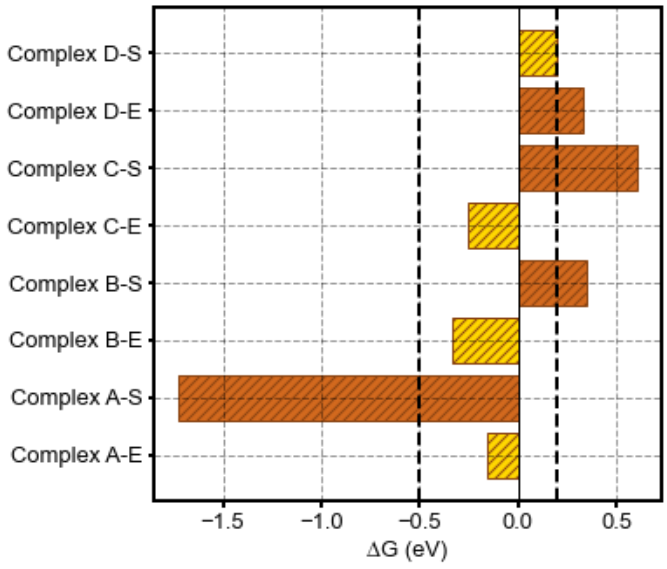

Figure 4. The computed *N_2 free energy of adsorption, ΔG_{N2}, on all of the studied complexes. The gold color represents the Fe atom with the ΔG_{N2} in the optimum range (0.2 to -0.5 eV), and the brown color represents the ΔG_{N2} values, not in the optimal range. The vertical dashed lines represent the optimum range of adsorption.

NRR on FeN_4C_8 and FeN_4C_{10}

In each hydrogenation step, an H^+/e^- pairs react with the N_xH_y (x=1,2; y=0-5) moieties and finally,

the NRR ends with the formation of $*NH_3$ above the FeN_4 active site. It is known that an ideal electrocatalyst can promote NRR when its potential exceeds the equilibrium potential without overpotential. Therefore, an electrocatalyst with lower overpotential is considered as a more ideal catalyst. We explored NRR steps for N_2 conversion to NH_3 in three pathways, namely, distal, alternating, and enzymatic [62-63], all of which involve N_2 adsorption as a prerequisite for the electrocatalytic NRR (see Scheme 1). In the distal and alternating pathways, the N_2 molecule adsorbs via the end-on orientation on the Fe center while the side-on adsorption of $*N_2$ is required for the enzymatic mechanism (Figure 2).

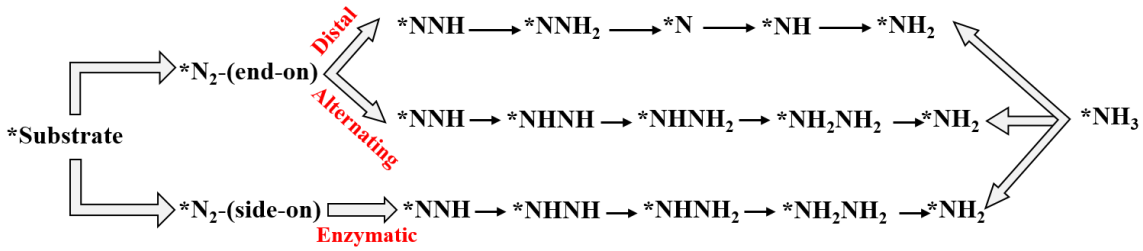

Scheme 1. Schematic view of possible pathways for NRR on Fe-N-C catalyst

Upon adsorption of NRR intermediates on the Fe atom, the oxidation state of the Fe atom changes from Fe^{II} to Fe^{III} [34]. During the NRR, the four Fe-N bond lengths of complexes A and B increase and divide into two pairs with two different bond lengths while they were identical in the pristine complexes. As a result of this bond elongation, the Fe atom slightly protrudes from the surface. Changes in the average Fe-N bond length are monitored during the reduction reaction in all three mechanisms and listed in Table S2. Depending on the catalyst and the corresponding mechanism, the Fe-N distance increases by about 1-9% during the NRR. The highest and lowest iron displacement corresponds to complex A in distal and alternating mechanisms, respectively. This slight movement is in close agreement with other fivefold-coordinated transition metal complexes [64] confirmed experimentally for ORR [20].

In distal and alternating mechanisms, the N_2 molecule with end-on orientation binds to the single Fe^{II} atom of complexes A and B with an adsorption energy of -0.61 and -0.71 eV, respectively. The

optimized stationary configurations of the nitrogen hydrogenation step on complexes A and B via distal and alternating routes along with their free energy diagrams are shown in Figures 5 and S2, respectively. One can see in Figure 5 that if NRR proceeds via the distal pathway on complex A, the only uphill step is the hydrogenation of *NNH to *NNH_2 with ΔG_{max} = 0.42 eV (see the red dash line in Figure 5). In the similar route on complex B, the first and second hydrogenation steps are uphill, with the calculated ΔG_{max} value of 1.33 and 0.93 eV, respectively. Contrary to complex B, the desorption of *NH_3 from Fe^{III} atom in complex A needs to overcome larger free energy of 2.39 eV while it is negligible on complex B (0.03 eV). However, according to experimental data, this process is not considered as a potential determining step (PDS) and is exergonic under acidic conditions because the adsorbed *NH_3 converts to NH_4^+ by reacting with H^+ in an acidic electrochemical environment, and does not directly desorb from the surface to form gaseous NH_3 [65-66]. Furthermore, the energy released in the hydrogenation process can overcome the energy required to release the second *NH_3 molecule from the surface. Thus, the corresponding limiting potential (U_L) for NRR on complexes A and B via the distal pathway is U_L = -0.42 V and -1.33 V vs SHE, respectively. The obtained value for the distal mechanism is in good agreement with that of the Mo-doped g-C_3N_4 catalyst [41].

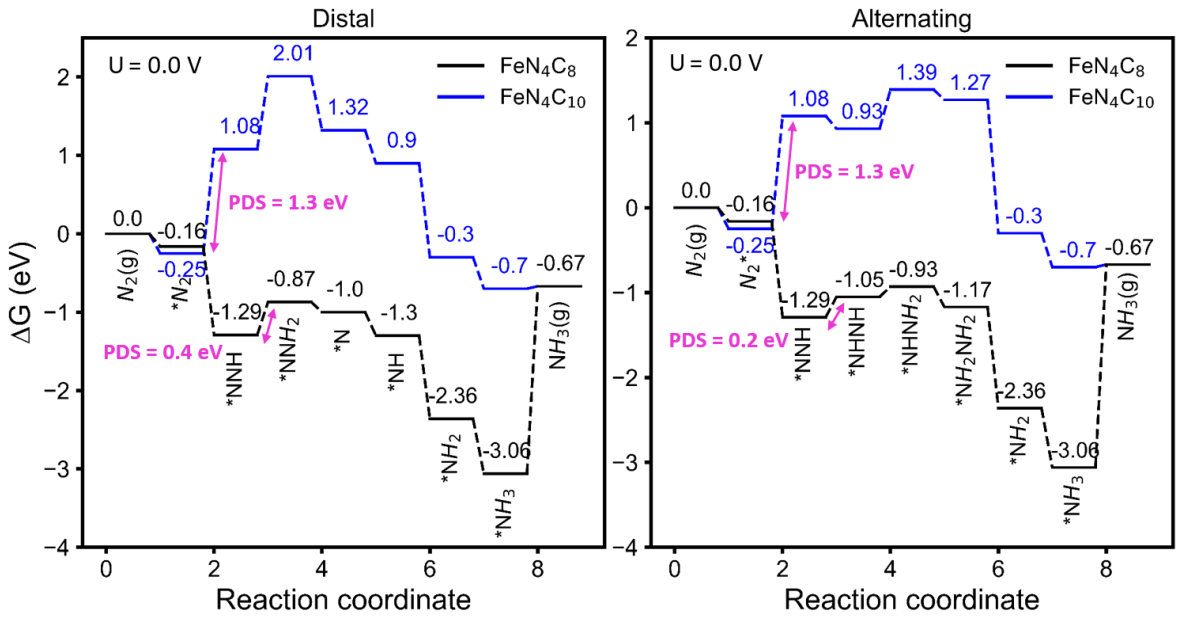

Figure 5. Comparison of the NRR through distal (left side) and alternating (right side) pathways on complexes A (black line) and B (blue line) at zero potential. The purple lines are the PDS steps.

Screening the NRR through the alternating mechanism on complex A, we found that the endergonic reactions correspond to the second and third hydrogenation steps, i.e., *NNH→*NHNH (ΔG_{max} = 0.24 eV) and *NHNH→*$NHNH_2$ (ΔG_{max} = 0.12 eV), respectively. The remaining hydrogenation steps are all downhill (see Figure 5). On complex B, the main uphill steps are for the hydrogenation of *N_2 →*NNH and*NHNH→*$NHNH_2$ with calculated ΔG_{max} values of 1.33 and 0.46 eV, respectively. Thus, the calculated limiting the potential for an alternating pathway on complex A (B) is U_L = -0.24 (-1.33) V vs SHE. Our results indicate that although both catalysts show good catalytic activity for NRR due to the low onset potentials, complex A tends to catalyze the NRR with a significantly lower U_L and overpotential ((U_L = -0.24 V, η=0.08 V vs SHE) than those of complex B (U_L = -1.33 V, η=1.17 V vs SHE). The obtained U_L is significantly lower than those previously reported for FeN_2, U_L = -1.16 V, Fe_2N_2 doped graphene, U_L = -0.39 V [67], and for Fe, FeN, FeN_2, and FeN_3 doped graphene with limiting potentials of -1.37, -1.16, -0.80, and -0.66 V, respectively [22].

NRR on fivefold-coordinated FeN_4C_8 and FeN_4C_{10}

To evaluate the reductive performance of electrocatalytic NRR on complexes C and D, we calculated the limiting potential for all mechanisms. Upon ligand adsorption on the pure catalyst, the Fe oxidation state changes from Fe^{II} to Fe^{III} as discussed above. When the NRR intermediates adsorb on Fe, its oxidation state changes [34], and consequently, the Fe atom pulls back into the N-plane by the ligand restoring the planarity of the FeN_4C_x catalyst.

According to Figure 4, we considered end-on and side-on N_2 adsorption on complexes C and D for NRR, respectively. We found that in the presence of the NH_2 ligand, the electrocatalytic NRR activity of complexes drastically decreases compared to the ligand-free structures (see Figures S4, S5, and S6). Once the NRR takes place on complex C and D via the distal and alternating pathways forming six-fold-coordinated configurations, the calculated onset potential increases drastically to U_L= -1.54 V and -1.59 V vs SHE, respectively. The enzymatic mechanism has the highest onset potential of -1.82 V vs HSE on complex C so we ignore this mechanism to occur at ambient conditions on this complex. On complex D,

the presence of the NH_2 ligand prohibits the complex D to proceed with NRR through the enzymatic pathway which might be due to the physisorbed N_2 molecule above the FeN_4 site (see Figure 2).

Comparing the NRR on two complexes we can estimate that the ligand has a significant effect on the whole NRR process. One can see in Figure S4 that it affects all the hydrogenation reactions on complexes A and B. The presence of the ligand shifts the free energy levels and also it changes the PDS reactions. On complex A, the PDS is related to the second hydrogenation step while on complex C the $*N_2$ hydrogenation is the PDS. Unlike NRR on complexes A (C), the energy shift slightly occurs on complex D while the PDS reactions are all related to the first hydrogenation reaction. Therefore, we confirm that the presence of the ligand influences the studied electrocatalysts reducing their activity for NRR. The reason may be related to the electron donation of N atoms which makes the FeN_5 center negative and consequently unfavorable for NRR.

^{57}Fe Mössbauer spectroscopy

^{57}Fe Mössbauer spectroscopy is a well-known method for the determination of the local electronic structure and coordination of iron nuclei in materials containing Fe atoms in their active sites [68-69]. The quadrupole splitting energy (ΔE_{QS}) is an important Mössbauer parameter that is affected by changing the Fe oxidation state, spin state, or the chemical surrounding [70]. Since the studied structures are in close agreement with those reported for similar Fe-N-C structures [71-72], we believe our results are also accurate for the proposed FeN_4C_8 structures.

As was reported by Mineva et al. [71], the obtained ΔE_{QS} values for complexes containing $Fe^{(II)}N_4$ pyridinic moieties can be assigned to the experimental doublet D2 (ΔE_{QS}=1.7−3.3 $mm.s^{-1}$) with a low (S=0) or medium-spin state (S=1). We did not consider the high spin state (S=2) because the obtained Mössbauer parameter values for this spin state were never experimentally observed for Fe-N-C catalysts [73-74]. Thus, we calculated the ΔE_{QS} for the pure and the six-fold-coordinated $Fe^{(II)}N_4$ catalysts and reported the data in Table S3. Obtained ΔE_{QS} values for the studied complexes containing $Fe^{(II)}$ with S=0 spin state are in the range of the reported experimental ΔE_{QS} values, while in the pure catalysts, the

quadrupole energy for both S=0 and S=1 is close to the experimental value of 3.3 $mm.s^{-1}$. Thus, the low spin Fe^{II} (S=0) is assigned to the FeN_4 catalysts in pure and six-fold coordinated configurations.

By either adsorption of an NRR species (here an *NH moiety) or a ligand (here NH_2) the oxidation state of iron increases from Fe^{II} to Fe^{III}. The obtained ΔE_{QS} values for five-fold coordinated FeN_4 catalysts in S= 5/2 ($0.9<\Delta E_{QS}<1.2$ $mm.s^{-1}$), in close agreement with experimental values [71, 75-76] (see Table S4).

NRR selectivity

To better estimate the catalytic activity of the complexes for NRR, their selectivity for the competing reactions should be investigated carefully. As a coupling reaction to NRR, the hydrogen evolution reaction (HER, $2H^+ + 2\ e^- \rightarrow H_2$, $E^0 = 0$ V) should be suppressed to improve the selectivity of nitrogen fixation[77]. HER is an important issue that hinders the development of efficient electrocatalysts [55, 78]. In acidic conditions, HER consumes a significant amount of H^+/e^- pairs, and may occupy the same active sites of NRR electrocatalysts and produce H_2 at similar limiting potentials as for NRR, reducing the Faraday efficiency (FE) and inducing low selectivity [79-80]. Therefore, asses the selectivity of the studied complexes with and without the fifth ligand for NRR, also the HER competition reaction should be considered. Here, we investigate the possibility of HER on the catalysts in three different ways. The adsorption selectivity is one way to improve overall NRR selectivity [81-82]. One can see in Figure 6a that for most of the studied complexes, the end-on N_2 adsorption is thermodynamically preferable to either side-on $*N_2$ or *H adsorption, except for complex A which tends to actively adsorb *H (-2.06 eV) rather than side-on (-1.73 eV) or end-on (-0.16 eV) $*N_2$. Moreover, the side-on orientation of $*N_2$ on complexes B and C along with both end-on and side-on orientations on complex D are thermodynamically unfavorable at ambient conditions. Thus, the HER reaction may outcompete the NRR on complex A. To further evaluate our results, we plotted the *H vs $*N_2$ free energy of adsorption considering the $*N_2$ side-on adsorption as a more energetically favorable configuration on complex D. As shown in Figure 6b, the catalysts in the blue region have a better NRR selectivity. As expected, despite the low NRR onset

potentials, complex A shows a larger tendency for HER reaction than NRR. Therefore, complex A could not be considered as a suitable electrocatalyst for NRR. Finally, we evaluate the selectivity of each catalyst toward HER and NRR by computing the corresponding limiting potentials of HER (U_L(HER)) for each system. The calculated U_L(HER) on complxes A, B, C, and D is 2.06, -0.16, -025, and -0.89 V, respectively, suggesting the poor HER performance on all complexes except for complex A. We further calculated the U_L (NRR) – U_L (HER) as shown in Figure 6c [55, 78]. It is known that the less negative U_L (NRR) – U_L (HER) values indicate higher NRR selectivity while our computed results are all in the negative region. According to Figure 6a, NRR is more active on the studied complexes in the order of complex D > complex C > complex B > complex A. The NRR limiting potential of distal and alternating mechanisms is considered for all complexes except for complex A, for which we considered the lowest U_L that is related to the alternating mechanism. Complexes B, C, and D can be considered as NRR active catalysts, from which complex B is confirmed to be NRR active due to the lower onset potential of -1.33 V vs HSE.

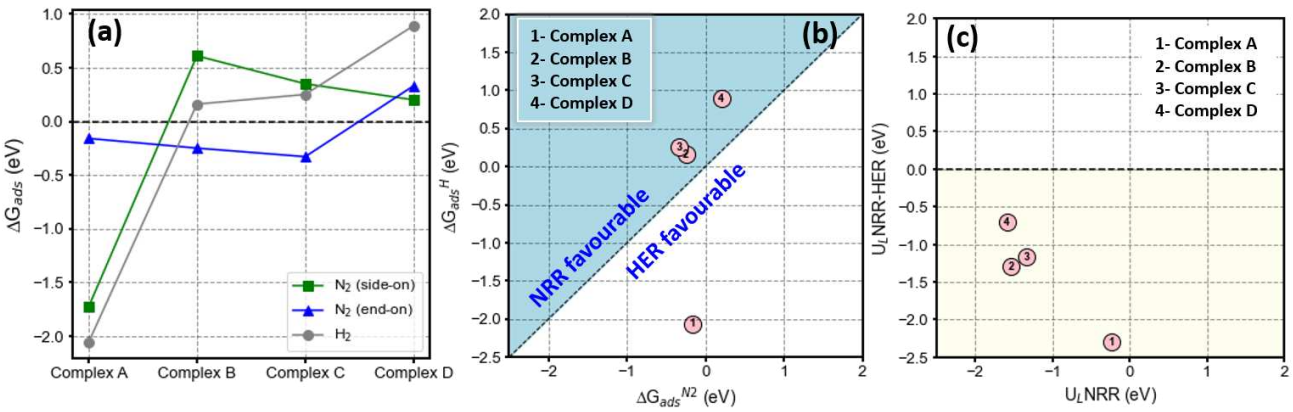

Figure 6. *N_2 and *H adsorption free energy (a), the free energy changes of *H adsorption vs *N_2 adsorption (b), and the difference between the U_L(NRR) and U_L(HER) (c) on complexes A-D

Thus, we here show that although FeN_4C_8 is expected to be a more active catalyst for NRR than the traditional pyridinic FeN_4C_{10} catalyst with a very low limiting potential of -0.24 V vs HSE, the HER outcompetes the NRR and therefore reduces the possibility of NRR to occur on this catalyst (see Figure 7). However, as proposed by Dodelet et al. [45] utilizing similar catalysts for ORR, we hereby

confirm that Fe^{II} is a representative ion of FeN_4C_8 and FeN_4C_{10} catalysts toward NRR at 0V potential. Finally, we concluded that although HER outcompetes the NRR on complex A, the negligible overpotential required for NRR on this catalyst can make it a good candidate for further catalytic and energy conversion investigations.

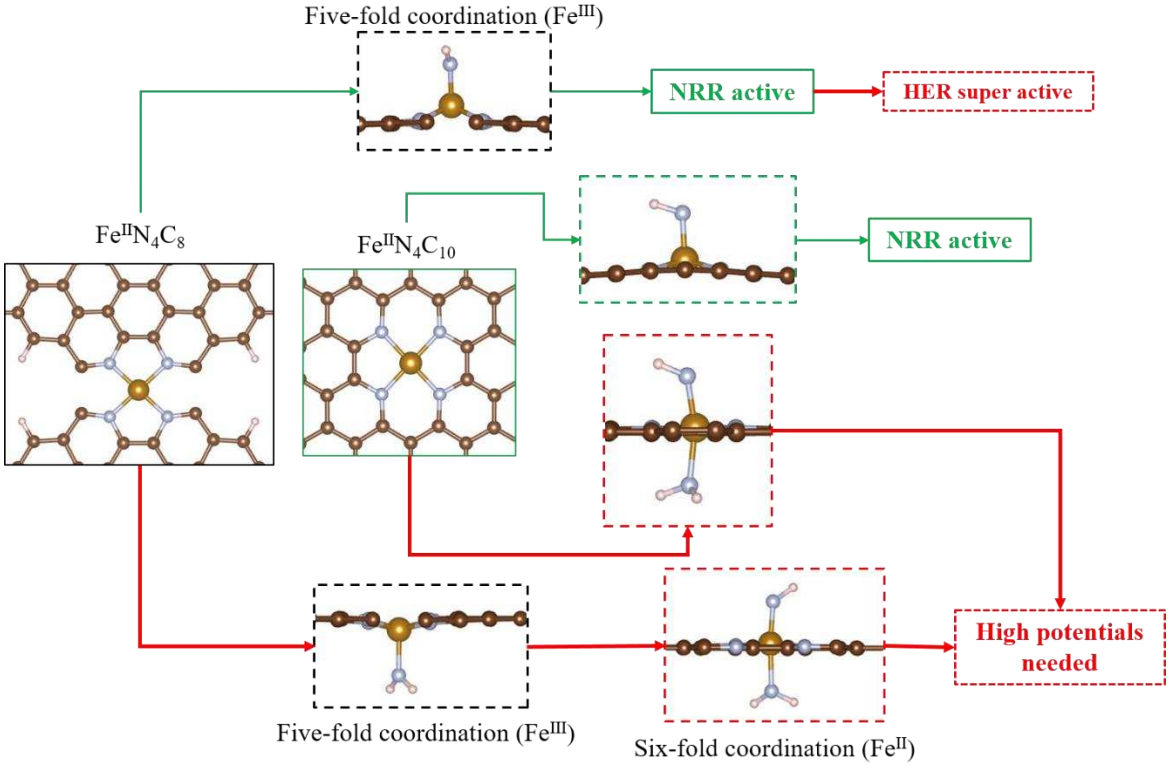

Figure 7. Visualization of the NRR on FeN_4C_8 and FeN_4C_{10} catalysts. During the reduction process, the four-fold coordination of $Fe^{II}N_4C_8$ changes to five-fold coordination $Fe^{III}N_4C_8$, and the NRR activity increases. In the presence of the ligand ($\mathbf{NH_2^-}$) the oxidation number of Fe^{II} does not change while the NRR activity of the catalyst decreases drastically. Color code: brown, C; blue, N; orange, Fe; and white, H.

Conclusion

Based on DFT and Mössbauer spectroscopy calculations, we propose that the traditional pyridinic $Fe^{II}N_4C_{10}$ has higher catalytic activity and selectivity for NRR than the robust $Fe^{II}N_4C_8$ catalyst. Notably, our study indicated that against the previously proposed ligand effect and Fe switching behavior [20], the FeN_4C_x monolayer with NH_2 functional ligand exhibits low catalytic applications on the NRR, while they suppress the HER for the NRR yielding ammonia. Using Mössbauer calculations we confirmed the changes in the iron oxidation number during the NRR process which were in good

accordance with the reported experimental data. The derived results can inspire more theoretical and experimental designs of different FeN_4 catalysts with different C topologies for different catalytic and electrocatalytic gas conversions.

Supporting Information

Mössbauer calculations; Quadrupole splitting and Isomer shift; The total density of state (TDOS) plots for complex A (top) and B (bottom); The most stable optimized adsorption configurations of NRR intermediate species through distal and alternating mechanisms on FeN_4C_8 and FeN_4C_{10} complexes. Color code: brown, C; blue, N; orange, Fe; and white, H; (a) The free energy diagram of the NRR through the enzymatic pathway on complexes A (black line) and B (blue line) at zero and applied potential. The PDS steps are shown in pink color. (b) The corresponding optimized adsorption configurations of the NRR intermediates on complexes A and B. Color code: brown, C; blue, N; orange, Fe; and white, H; Comparison of the distal and alternating mechanisms on complexes A with C (top) with complexes B and D (bottom) at zero potential. The pink lines are the PDS steps; The optimized configurations of NRR intermediates on complex C through the distal, alternating, and enzymatic pathways. Color code: brown, C; blue, N; orange, Fe; and white, H; The optimized configurations of NRR intermediates on complex D through distal and alternating pathways. Color code: brown, C; blue, N; orange, Fe; and white, H; The computed average N-N bond length (dN-N) of adsorbed $*N_2$ on complexes A, B, C, and D along with the corresponding adsorption energy (E_{ads}) of $*N_2$ and *H; The computed average Fe-N bond length (d_{Fe-N}) of NRR intermediates, the adsorption energy (E_{ads}) of the Fe atom, the calculated NRR limiting potential (U_{lim}), and overpotential (η) on each complex in distal, alternating and enzymatic mechanism.Quadrupole splitting energy (ΔE_{QS}) in $mm.s^{-1}$ for the catalysts containing ferrous moieties; Quadrupole splitting energy (ΔE_{QS}) in $mm.s^{-1}$ for the catalysts containing ferric moieties.

Acknowledgments

The authors gratefully acknowledge the financial support from the Fund of Scientific Research Flanders (FWO), Belgium, Grant number 1261721N. The computational resources and services used in this work were provided by the HPC core facility CalcUA of the Universiteit Antwerpen and VSC (Flemish Supercomputer Center), funded by the FWO and the Flemish Government.

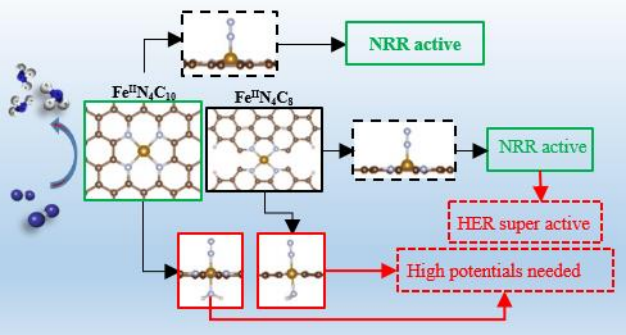

Graphical abstract: Effects of the ligand and C topologies on electrochemical N_2 reduction on Fe-N_4-C_x (x=3,8,10) catalysts

References

1. Geng, Z.; Liu, Y.; Kong, X.; Li, P.; Li, K.; Liu, Z.; Du, J.; Shu, M.; Si, R.; Zeng, J., Achieving a Record ‐ High Yield Rate of 120.9 for N2 Electrochemical Reduction over Ru Single ‐ Atom Catalysts. *Adv. Mater.* **2018**, *30*, 1803498.
2. Han, J.; Liu, Z.; Ma, Y.; Cui, G.; Xie, F.; Wang, F.; Wu, Y.; Gao, S.; Xu, Y.; Sun, X., Ambient N2 Fixation to Nh3 at Ambient Conditions: Using Nb2o5 Nanofiber as a High-Performance Electrocatalyst. *Nano Energy* **2018**, *52*, 264-270.
3. Ji, S.; Wang, Z.; Zhao, J., A Boron-Interstitial Doped C 2 N Layer as a Metal-Free Electrocatalyst for N 2 Fixation: A Computational Study. *J. Mater. Chem. A* **2019**, *7*, 2392-2399.
4. Adekoya, D.; Qian, S.; Gu, X.; Wen, W.; Li, D.; Ma, J.; Zhang, S., Dft-Guided Design and Fabrication of Carbon-Nitride-Based Materials for Energy Storage Devices: A Review. *Nano-Micro Letters* **2021**, *13*, 1-44.
5. Qiu, H. J.; Ito, Y.; Cong, W.; Tan, Y.; Liu, P.; Hirata, A.; Fujita, T.; Tang, Z.; Chen, M., Nanoporous Graphene with Single ‐ Atom Nickel Dopants: An Efficient and Stable Catalyst for Electrochemical Hydrogen Production. *Angew. Chem.* **2015**, *54*, 14031-14035.
6. Zhang, Z.; Xiao, J.; Chen, X. J.; Yu, S.; Yu, L.; Si, R.; Wang, Y.; Wang, S.; Meng, X.; Wang, Y., Reaction Mechanisms of Well ‐ Defined Metal ‐ N4 Sites in Electrocatalytic Co2 Reduction. *Angew. Chem.* **2018**, *57*, 16339-16342.
7. Niu, H.; Zhang, Z.; Wang, X.; Wan, X.; Shao, C.; Guo, Y., Theoretical Insights into the Mechanism of Selective Nitrate ‐ to ‐ Ammonia Electroreduction on Single ‐ Atom Catalysts. *Adv. Funct. Mater.* **2021**, *31*, 2008533.
8. Svane, K. L.; Reda, M.; Vegge, T.; Hansen, H. A., Improving the Activity of M− N4 Catalysts for the Oxygen Reduction Reaction by Electrolyte Adsorption. *ChemSusChem* **2019**, *12*, 5133-5141.
9. Abel, M.; Clair, S.; Ourdjini, O.; Mossoyan, M.; Porte, L., Single Layer of Polymeric Fe-Phthalocyanine: An Organometallic Sheet on Metal and Thin Insulating Film. *Journal of the American Chemical Society* **2011**, *133*, 1203-1205.
10. Wu, G., Current Challenge and Perspective of Pgm-Free Cathode Catalysts for Pem Fuel Cells. *Frontiers in Energy* **2017**, *11*, 286-298.
11. He, Y.; Tan, Q.; Lu, L.; Sokolowski, J.; Wu, G., Metal-Nitrogen-Carbon Catalysts for Oxygen Reduction in Pem Fuel Cells: Self-Template Synthesis Approach to Enhancing Catalytic Activity and Stability. *Electrochemical Energy Reviews* **2019**, *2*, 231-251.
12. Chen, J.; Yan, X.; Fu, C.; Feng, Y.; Lin, C.; Li, X.; Shen, S.; Ke, C.; Zhang, J., Insight into the Rapid Degradation Behavior of Nonprecious Metal Fe-N-C Electrocatalyst-Based Proton Exchange Membrane Fuel Cells. *ACS Appl. Mater. Interfaces* **2019**, *11*, 37779-37786.
13. Lefèvre, M.; Proietti, E.; Jaouen, F.; Dodelet, J.-P., Iron-Based Catalysts with Improved Oxygen Reduction Activity in Polymer Electrolyte Fuel Cells. *Science* **2009**, *324*, 71-74.
14. Melville, O. A.; Lessard, B. H.; Bender, T. P., Phthalocyanine-Based Organic Thin-Film Transistors: A Review of Recent Advances. *ACS Appl. Mater. Interfaces* **2015**, *7*, 13105-13118.
15. Anderson, A. B.; Holby, E. F., Pathways for O2 Electroreduction over Substitutional Fen4, Hofen4, and Ofen4 in Graphene Bulk Sites: Critical Evaluation of Overpotential Predictions Using Lger and Che Models. *J. Phys. Chem. C.* **2019**, *123*, 18398-18409.
16. Han, Y.; Wang, Y.; Xu, R.; Chen, W.; Zheng, L.; Han, A.; Zhu, Y.; Zhang, J.; Zhang, H.; Luo, J., Electronic Structure Engineering to Boost Oxygen Reduction Activity by Controlling the Coordination of the Central Metal. *Energy Environ. Sci.* **2018**, *11*, 2348-2352.
17. Li, X.-F.; Li, Q.-K.; Cheng, J.; Liu, L.; Yan, Q.; Wu, Y.; Zhang, X.-H.; Wang, Z.-Y.; Qiu, Q.; Luo, Y., Conversion of Dinitrogen to Ammonia by Fen3-Embedded Graphene. *Journal of the American Chemical Society* **2016**, *138*, 8706-8709.
18. Liu, S.; Liu, Y.; Cheng, Z.; Tan, Y.; Ren, Y.; Yuan, T.; Shen, Z., Catalytic Role of Adsorption

of Electrolyte/Molecules as Functional Ligands on Two-Dimensional Tm-N4 Monolayer Catalysts for the Electrocatalytic Nitrogen Reduction Reaction. *ACS Appl. Mater. Interfaces* **2021**, *13*, 40590-40601.
19. Wang, Q.; Zhou, Z.-Y.; Lai, Y.-J.; You, Y.; Liu, J.-G.; Wu, X.-L.; Terefe, E.; Chen, C.; Song, L.; Rauf, M., Phenylenediamine-Based Fen X/C Catalyst with High Activity for Oxygen Reduction in Acid Medium and Its Active-Site Probing. *Journal of the American chemical Society* **2014**, *136*, 10882-10885.
20. Jia, Q.; Ramaswamy, N.; Hafiz, H.; Tylus, U.; Strickland, K.; Wu, G.; Barbiellini, B.; Bansil, A.; Holby, E. F.; Zelenay, P., Experimental Observation of Redox-Induced Fe–N Switching Behavior as a Determinant Role for Oxygen Reduction Activity. *ACS Nano* **2015**, *9*, 12496-12505.
21. Brown, K. A.; Harris, D. F.; Wilker, M. B.; Rasmussen, A.; Khadka, N.; Hamby, H.; Keable, S.; Dukovic, G.; Peters, J. W.; Seefeldt, L. C., Light-Driven Dinitrogen Reduction Catalyzed by a Cds: Nitrogenase Mofe Protein Biohybrid. *Science* **2016**, *352*, 448-450.
22. Guo, X.; Huang, S., Tuning Nitrogen Reduction Reaction Activity Via Controllable Fe Magnetic Moment: A Computational Study of Single Fe Atom Supported on Defective Graphene. *Electrochim. Acta* **2018**, *284*, 392-399.
23. Shan, W.; Wang, G., Enhancing Catalytic Properties of Iron-and Nitrogen-Doped Carbon for Nitrogen Reduction through Structural Distortion: A Density Functional Theory Study. *J. Phys. Chem. C.* **2021**, *125*, 16004-16012.
24. Wang, Y.; Cui, X.; Zhao, J.; Jia, G.; Gu, L.; Zhang, Q.; Meng, L.; Shi, Z.; Zheng, L.; Wang, C., Rational Design of Fe–N/C Hybrid for Enhanced Nitrogen Reduction Electrocatalysis under Ambient Conditions in Aqueous Solution. *ACS Catal.* **2018**, *9*, 336-344.
25. Kresse, G.; Hafner, J., Ab Initio Molecular Dynamics for Liquid Metals. *Phys. Rev. B* **1993**, *47*, 558.
26. Perdew, J.; Burke, K.; Ernzerhof, M., D. Of Physics and Nol 70118 J. Quantum Theory Group Tulane University. *Phys. Rev. Lett* **1996**, *77*, 3865-3868.
27. Kresse, G.; Furthmüller, J., Efficiency of Ab-Initio Total Energy Calculations for Metals and Semiconductors Using a Plane-Wave Basis Set. *Comput. Mater. Sci.* **1996**, *6*, 15-50.
28. Perdew, J. P.; Chevary, J. A.; Vosko, S. H.; Jackson, K. A.; Pederson, M. R.; Singh, D. J.; Fiolhais, C., Atoms, Molecules, Solids, and Surfaces: Applications of the Generalized Gradient Approximation for Exchange and Correlation. *Phys. Rev. B* **1992**, *46*, 6671.
29. Blöchl, P. E., Projector Augmented-Wave Method. *Phys. Rev. B* **1994**, *50*, 17953.
30. Bucko, T.; Hafner, J.; Lebegue, S.; Angyán, J. G., Improved Description of the Structure of Molecular and Layered Crystals: Ab Initio Dft Calculations with Van Der Waals Corrections. *J. Phys. Chem. A.* **2010**, *114*, 11814-11824.
31. Wang, M.; Wang, Z., Single Ni Atom Incorporated with Pyridinic Nitrogen Graphene as an Efficient Catalyst for Co Oxidation: First-Principles Investigation. *RSC Adv.* **2017**, *7*, 48819-48824.
32. Lin, Y.-C.; Teng, P.-Y.; Yeh, C.-H.; Koshino, M.; Chiu, P.-W.; Suenaga, K., Structural and Chemical Dynamics of Pyridinic-Nitrogen Defects in Graphene. *Nano Lett.* **2015**, *15*, 7408-7413.
33. Luo, Z.; Lim, S.; Tian, Z.; Shang, J.; Lai, L.; MacDonald, B.; Fu, C.; Shen, Z.; Yu, T.; Lin, J., Pyridinic N Doped Graphene: Synthesis, Electronic Structure, and Electrocatalytic Property. *J. Mater. Chem.* **2011**, *21*, 8038-8044.
34. Rovira, C.; Kunc, K.; Hutter, J.; Ballone, P.; Parrinello, M., Equilibrium Geometries and Electronic Structure of Iron− Porphyrin Complexes: A Density Functional Study. *J. Phys. Chem. A.* **1997**, *101*, 8914-8925.
35. Momma, K.; Izumi, F., Vesta: A Three-Dimensional Visualization System for Electronic and Structural Analysis. *Journal of Applied crystallography* **2008**, *41*, 653-658.
36. Monkhorst, H. J.; Pack, J. D., Special Points for Brillouin-Zone Integrations. *Phys. Rev. B* **1976**, *13*, 5188.
37. Tang, W.; Sanville, E.; Henkelman, G., A Grid-Based Bader Analysis Algorithm without

Lattice Bias. *J. Phys. Condens. Matter* **2009**, *21*, 084204.
38. Nørskov, J. K.; Rossmeisl, J.; Logadottir, A.; Lindqvist, L.; Kitchin, J. R.; Bligaard, T.; Jonsson, H., Origin of the Overpotential for Oxygen Reduction at a Fuel-Cell Cathode. *J. Phys. Chem. B.* **2004**, *108*, 17886-17892.
39. Peterson, A. A.; Abild-Pedersen, F.; Studt, F.; Rossmeisl, J.; Nørskov, J. K., How Copper Catalyzes the Electroreduction of Carbon Dioxide into Hydrocarbon Fuels. *Energy Environ. Sci.* **2010**, *3*, 1311-1315.
40. Wang, V.; Xu, N.; Liu, J.-C.; Tang, G.; Geng, W.-T., Vaspkit: A User-Friendly Interface Facilitating High-Throughput Computing and Analysis Using Vasp Code. *Computer Physics Communications* **2021**, *267*, 108033.
41. Agarwal, S.; Kumar, R.; Arya, R.; Singh, A. K., Rational Design of Single-Atom Catalysts for Enhanced Electrocatalytic Nitrogen Reduction Reaction. *J. Phys. Chem. C.* **2021**, *125*, 12585-12593.
42. Cao, Y.; Deng, S.; Fang, Q.; Sun, X.; Zhao, C.; Zheng, J.; Gao, Y.; Zhuo, H.; Li, Y.; Yao, Z., Single and Double Boron Atoms Doped Nanoporous C2n–H2d Electrocatalysts for Highly Efficient N2 Reduction Reaction: A Density Functional Theory Study. *Nanotechnology* **2019**, *30*, 335403.
43. Deng, C.; He, R.; Wen, D.; Shen, W.; Li, M., Theoretical Study on the Origin of Activity for the Oxygen Reduction Reaction of Metal-Doped Two-Dimensional Boron Nitride Materials. *Phys. Chem. Chem. Phys.* **2018**, *20*, 10240-10246.
44. Chen, X.; Chen, S.; Wang, J., Screening of Catalytic Oxygen Reduction Reaction Activity of Metal-Doped Graphene by Density Functional Theory. *Appl. Surf. Sci.* **2016**, *379*, 291-295.
45. Lefèvre, M.; Dodelet, J.; Bertrand, P., Molecular Oxygen Reduction in Pem Fuel Cells: Evidence for the Simultaneous Presence of Two Active Sites in Fe-Based Catalysts. *J. Phys. Chem. B.* **2002**, *106*, 8705-8713.
46. Zagal, J. H.; Bedioui, F.; Dodelet, J.-P., *N4-Macrocyclic Metal Complexes*; Springer Science & Business Media, 2007.
47. Bouwkamp-Wijnoltz, A.; Visscher, W.; Van Veen, J.; Boellaard, E.; Van der Kraan, A.; Tang, S., On Active-Site Heterogeneity in Pyrolyzed Carbon-Supported Iron Porphyrin Catalysts for the Electrochemical Reduction of Oxygen: An in Situ Mössbauer Study. *J. Phys. Chem. B.* **2002**, *106*, 12993-13001.
48. Lefevre, M.; Dodelet, J.; Bertrand, P., O2 Reduction in Pem Fuel Cells: Activity and Active Site Structural Information for Catalysts Obtained by the Pyrolysis at High Temperature of Fe Precursors. *J. Phys. Chem. B.* **2000**, *104*, 11238-11247.
49. Bron, M.; Fiechter, S.; Hilgendorff, M.; Bogdanoff, P., Catalysts for Oxygen Reduction from Heat-Treated Carbon-Supported Iron Phenantroline Complexes. *J. Appl. Electrochem.* **2002**, *32*, 211-216.
50. Bron, M.; Radnik, J.; Fieber-Erdmann, M.; Bogdanoff, P.; Fiechter, S., Exafs, Xps and Electrochemical Studies on Oxygen Reduction Catalysts Obtained by Heat Treatment of Iron Phenanthroline Complexes Supported on High Surface Area Carbon Black. *Journal of Electroanalytical Chemistry* **2002**, *535*, 113-119.
51. Bron, M.; Fiechter, S.; Bogdanoff, P.; Tributsch, H., Thermogravimetry/Mass Spectrometry Investigations on the Formation of Oxygen Reduction Catalysts for Pem Fuel Cells on the Basis of Heat ‐ Treated Iron Phenanthroline Complexes. *Fuel Cells* **2002**, *2*, 137-142.
52. Holby, E. F.; Zelenay, P., Linking Structure to Function: The Search for Active Sites in Non-Platinum Group Metal Oxygen Reduction Reaction Catalysts. *Nano Energy* **2016**, *29*, 54-64.
53. Szakacs, C. E.; Lefèvre, M.; Kramm, U. I.; Dodelet, J.-P.; Vidal, F., A Density Functional Theory Study of Catalytic Sites for Oxygen Reduction in Fe/N/C Catalysts Used in H 2/O 2 Fuel Cells. *Phys. Chem. Chem. Phys.* **2014**, *16*, 13654-13661.
54. Skulason, E.; Bligaard, T.; Gudmundsdóttir, S.; Studt, F.; Rossmeisl, J.; Abild-Pedersen, F.; Vegge, T.; Jónsson, H.; Nørskov, J. K., A Theoretical Evaluation of Possible Transition Metal Electro-Catalysts for N 2 Reduction. *Phys. Chem. Chem. Phys.* **2012**, *14*, 1235-1245.

55. Montoya, J. H.; Tsai, C.; Vojvodic, A.; Nørskov, J. K., The Challenge of Electrochemical Ammonia Synthesis: A New Perspective on the Role of Nitrogen Scaling Relations. *ChemSusChem* **2015**, *8*, 2180-2186.
56. Niu, H.; Wang, X.; Shao, C.; Zhang, Z.; Guo, Y., Computational Screening Single-Atom Catalysts Supported on G-Cn for N2 Reduction: High Activity and Selectivity. *ACS Sustainable Chemistry & Engineering* **2020**, *8*, 13749-13758.
57. Légaré, M.-A.; Bélanger-Chabot, G.; Dewhurst, R. D.; Welz, E.; Krummenacher, I.; Engels, B.; Braunschweig, H., Nitrogen Fixation and Reduction at Boron. *Science* **2018**, *359*, 896-900.
58. Sabatier, P., *La Catalyse En Chimie Organique*, 1920.
59. Song, W.; Xie, K.; Wang, J.; Guo, Y.; He, C.; Fu, L., Density Functional Theory Study of Transition Metal Single-Atoms Anchored on Graphyne as Efficient Electrocatalysts for the Nitrogen Reduction Reaction. *Phys. Chem. Chem. Phys.* **2021**, *23*, 10418-10428.
60. Ji, Y.; Li, Y.; Dong, H.; Ding, L.; Li, Y., Ruthenium Single-Atom Catalysis for Electrocatalytic Nitrogen Reduction Unveiled by Grand Canonical Density Functional Theory. *J. Mater. Chem. A* **2020**, *8*, 20402-20407.
61. Liu, F.; Song, L.; Liu, Y.; Zheng, F.; Wang, L.; Palotás, K.; Lin, H.; Li, Y., Using the N [Triple Bond, Length as M-Dash] N Dipole as a Theoretical Indicator for Estimating the Electrocatalytic Performance of Active Sites in the Nitrogen Reduction Reaction: Single Transition Metal Atoms Embedded in Two Dimensional Phthalocyanine. *J. Mater. Chem. A* **2020**, *8*, 3598-3605.
62. Cui, X.; Tang, C.; Zhang, Q., A Review of Electrocatalytic Reduction of Dinitrogen to Ammonia under Ambient Conditions. *Advanced Energy Materials* **2018**, *8*, 1800369.
63. Van der Ham, C. J.; Koper, M. T.; Hetterscheid, D. G., Challenges in Reduction of Dinitrogen by Proton and Electron Transfer. *Chem. Soc. Rev.* **2014**, *43*, 5183-5191.
64. Albright, T. A.; Burdett, J. K.; Whangbo, M.-H., *Orbital Interactions in Chemistry*; John Wiley & Sons, 2013.
65. Choi, C.; Back, S.; Kim, N.-Y.; Lim, J.; Kim, Y.-H.; Jung, Y., Suppression of Hydrogen Evolution Reaction in Electrochemical N2 Reduction Using Single-Atom Catalysts: A Computational Guideline. *ACS Catal.* **2018**, *8*, 7517-7525.
66. Chun, H.-J.; Apaja, V.; Clayborne, A.; Honkala, K.; Greeley, J., Atomistic Insights into Nitrogen-Cycle Electrochemistry: A Combined Dft and Kinetic Monte Carlo Analysis of No Electrochemical Reduction on Pt (100). *ACS Catal.* **2017**, *7*, 3869-3882.
67. Ma, D.; Zeng, Z.; Liu, L.; Huang, X.; Jia, Y., Computational Evaluation of Electrocatalytic Nitrogen Reduction on Tm Single-, Double-, and Triple-Atom Catalysts (Tm= Mn, Fe, Co, Ni) Based on Graphdiyne Monolayers. *J. Phys. Chem. C.* **2019**, *123*, 19066-19076.
68. Niemantsverdriet, J.; Van der Kraan, A.; Van Dijk, W.; Van der Baan, H., Behavior of Metallic Iron Catalysts During Fischer-Tropsch Synthesis Studied with Mossbauer Spectroscopy, X-Ray Diffraction, Carbon Content Determination, and Reaction Kinetic Measurements. *J. Phys. Chem.* **2002**, *84*, 3363-3370.
69. Blaha, P. In *Calculations of Mössbauer Parameters in Solids by Dft Bandstructure Calculations*, Journal of Physics: Conference Series, IOP Publishing: 2010; p 012009.
70. Che, M.; Védrine, J. C., *Characterization of Solid Materials and Heterogeneous Catalysts: From Structure to Surface Reactivity*; John Wiley & Sons, 2012.
71. Mineva, T.; Matanovic, I.; Atanassov, P.; Sougrati, M.-T.; Stievano, L.; Clémancey, M.; Kochem, A.; Latour, J.-M.; Jaouen, F., Understanding Active Sites in Pyrolyzed Fe–N–C Catalysts for Fuel Cell Cathodes by Bridging Density Functional Theory Calculations and 57fe Mossbauer Spectroscopy. *ACS Catal.* **2019**, *9*, 9359-9371.
72. Li, J.; Sougrati, M. T.; Zitolo, A.; Ablett, J. M.; Oğuz, I. C.; Mineva, T.; Matanovic, I.; Atanassov, P.; Huang, Y.; Zenyuk, I., Identification of Durable and Non-Durable Fen X Sites in Fe–N–C Materials for Proton Exchange Membrane Fuel Cells. *Nature Catalysis* **2021**, *4*, 10-19.
73. Kramm, U. I.; Herranz, J.; Larouche, N.; Arruda, T. M.; Lefevre, M.; Jaouen, F.; Bogdanoff,

P.; Fiechter, S.; Abs-Wurmbach, I.; Mukerjee, S., Structure of the Catalytic Sites in Fe/N/C-Catalysts for O 2-Reduction in Pem Fuel Cells. *Phys. Chem. Chem. Phys.* **2012**, *14*, 11673-11688.
74. Champion, P.; Chiang, R.; Münck, E.; Debrunner, P.; Hager, L., Mössbauer Investigations of High-Spin Ferrous Heme Proteins. Ii. Chloroperoxidase, Horseradish Peroxidase, and Hemoglobin. *Biochemistry* **1975**, *14*, 4159-4166.
75. Kramm, U. I.; Herrmann-Geppert, I.; Behrends, J.; Lips, K.; Fiechter, S.; Bogdanoff, P., On an Easy Way to Prepare Metal–Nitrogen Doped Carbon with Exclusive Presence of Men4-Type Sites Active for the Orr. *Journal of the American Chemical Society* **2016**, *138*, 635-640.
76. Sougrati, M. T.; Goellner, V.; Schuppert, A. K.; Stievano, L.; Jaouen, F., Probing Active Sites in Iron-Based Catalysts for Oxygen Electro-Reduction: A Temperature-Dependent 57fe Mössbauer Spectroscopy Study. *Catal. Today* **2016**, *262*, 110-120.
77. Seh, Z. W.; Kibsgaard, J.; Dickens, C. F.; Chorkendorff, I.; Nørskov, J. K.; Jaramillo, T. F., Combining Theory and Experiment in Electrocatalysis: Insights into Materials Design. *Science* **2017**, *355*, eaad4998.
78. Chen, Z.; Zhao, J.; Cabrera, C. R.; Chen, Z., Computational Screening of Efficient Single‐Atom Catalysts Based on Graphitic Carbon Nitride (G‐C3n4) for Nitrogen Electroreduction. *Small Methods* **2019**, *3*, 1800368.
79. Qing, G.; Ghazfar, R.; Jackowski, S. T.; Habibzadeh, F.; Ashtiani, M. M.; Chen, C.-P.; Smith III, M. R.; Hamann, T. W., Recent Advances and Challenges of Electrocatalytic N2 Reduction to Ammonia. *Chem. Rev.* **2020**, *120*, 5437-5516.
80. Singh, A.; Rohr, B.; Schwalbe, J.; Cargnello, M.; Chan, K.; Jaramillo, T., 464 Chorkendorff, I.; Nørskov, Jk, Electrochemical Ammonia Synthesis—the Selectivity Challenge. Acs 465. *Catalysis* **2017**, *7*, 706-709.
81. Tao, H.; Choi, C.; Ding, L.-X.; Jiang, Z.; Han, Z.; Jia, M.; Fan, Q.; Gao, Y.; Wang, H.; Robertson, A. W., Nitrogen Fixation by Ru Single-Atom Electrocatalytic Reduction. *Chem* **2019**, *5*, 204-214.
82. Zhao, W.; Zhang, L.; Luo, Q.; Hu, Z.; Zhang, W.; Smith, S.; Yang, J., Single Mo1 (Cr1) Atom on Nitrogen-Doped Graphene Enables Highly Selective Electroreduction of Nitrogen into Ammonia. *ACS Catal.* **2019**, *9*, 3419-3425.

Identification of A Unique Pyridinic FeN_4C_x Electrocatalyst For N_2 Reduction: Tailoring The Coordination And Carbon Topologies

Parisa Nematollahi[*a], Erik C. Neyts[a]

[a] Research Group Plasmant, NANO lab Center of Excellence, Department of Chemistry, University of Antwerp, Universiteitsplein 1, 2610 Antwerp, Belgium

* Corresponding author. **Phone:** (+32) 32652346. **E-mail**: parisa.nematollahi@uantwerpen.be

Mössbauer calculations

The electric field gradients (EFGs) at the positions of the Fe nuclei are calculated for all structures using VASP [1]. Cutoff energy of 400 eV and a Γ-point centered k-point mesh of 5×5×1 is chosen for the simulated models. Convergence of the total energy was calculated using an energy cutoff in the range of 300-900 eV and the k-point sampling used meshes from 1×1×1 to 9×9×1. In all cases, the Fermi-Dirac smearing method with a sigma value of 0.03 eV was used [2].

Quadrupole splitting and Isomer shift

The quadrupole splitting energy (ΔE_{QS}) can be obtained from the coupling between the nuclear quadrupole moment (Q) of the non-spherical nucleus and the principal components V_{ii} (I = x, y, z) of the EFG tensor at ^{57}Fe nucleus using:

$$\Delta E_{QS} = \frac{1}{2} eQV_{zz}\sqrt{1+\frac{\eta^2}{3}} \quad (1)$$

Here e and Q are the elementary charge and nuclear quadrupole moment, respectively. The quadrupole moment of the excited ^{57}Fe nucleus is about 0.16 barn (1barn = 10^{-28} m^2) [3]. The EFG asymmetry parameter (η) is defined as $\eta = (V_{xx} - V_{yy})/V_{zz}$ where $|V_{zz}| \geq |V_{yy}| \geq V_{xx}$. In order to compare the computed ΔE_{QS} values with the corresponding experimental data, ΔE_{QS} is reported in units of mm/s. Calculation of ΔE_{QS} and η involves a computation of the EFG through the value of the EFG operator, $V_{ij} = \langle \Psi_0 \left| \frac{3ij-r^2}{r^5} \right| \Psi_0 \rangle$, for the electronic ground state Ψ_0 with i, j = x, y, z denoting components of the electron radius vector r.

The isomer shift (IS), δ, always relates to the differences in electron density at the nucleus in the absorber (ρ_0^{sample}) and a reference ($\rho_0^{reference}$) compound (typically α-Fe). This parameter can be calculated as [4]:

$$\delta = \alpha(\rho_0^{sample} - \rho_0^{reference})$$

where α is the so-called calibration constant ($\alpha = -0.1573\alpha_0^3\ mm.s^{-1}$) which is determined from the experimental parameters of the ^{57}Fe nuclear transition [5] and ρ_0 is the nonrelativistic calculated total charge density at the iron nucleus. Both QS and IS arise from the interaction between the charge densities of the iron nucleus and the surrounding electrons. The QS gives information about the electric field gradient, that is, the degree of asymmetry within the electron density while IS gives the electron density at the iron nucleus also known as the contact density [6-7].

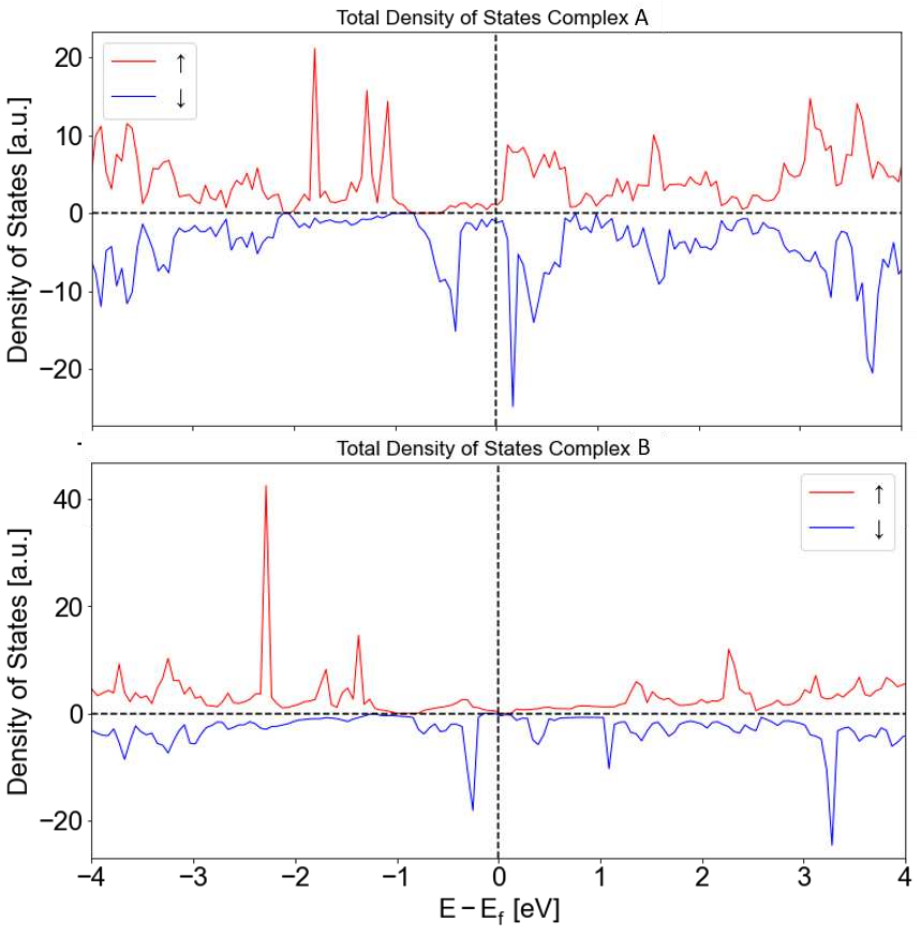

Figure S1. The total density of state (TDOS) plots for complex A (top) and B (bottom)

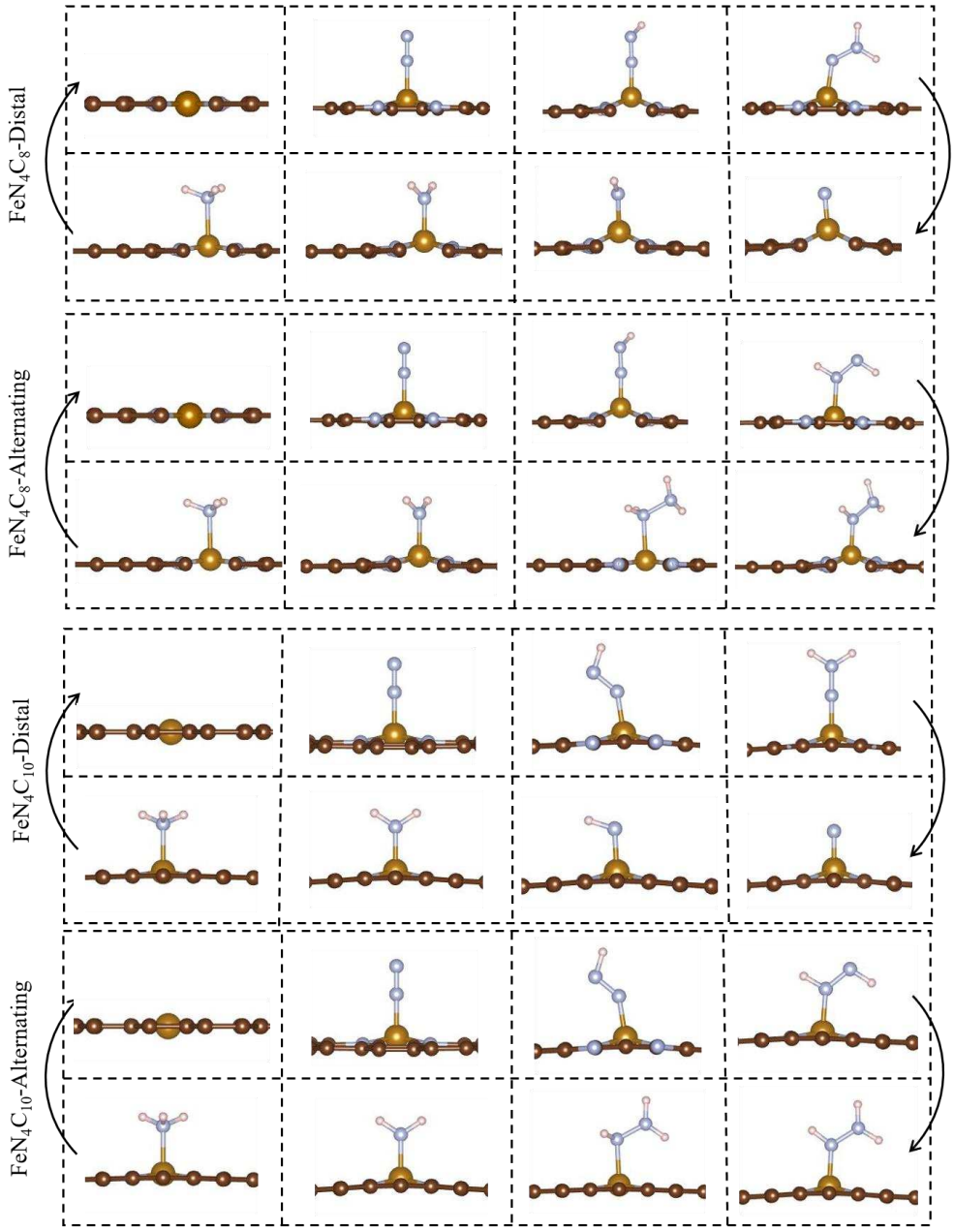

Figure S2. The most stable optimized adsorption configurations of NRR intermediate species through distal and alternating mechanisms on FeN_4C_8 and FeN_4C_{10} complexes. Color code: brown, C; blue, N; orange, Fe; and white, H.

The adsorption of the N_2 molecule on the FeN_4 site in the enzymatic mechanism is strongly exothermic on complex A while it is endothermic on complex B (see Figure S3). However, although all hydrogenation steps on complex A in the enzymatic pathway are downhill, the hydrogenation of $*N_2$ is endothermic with ΔG_{max} = 1.07 eV, indicating a slower reaction than for end-on configurations. On complex B the first three hydrogenation steps are uphill from which the formation of *NHNH is considered as the PDS, with ΔG_{max} = 0.70 eV.

Moreover, we find that in contrast to the alternating mechanism, the $d_{Fe\text{-}N}$ increases drastically in both distal and enzymatic pathways (see Table S2) which might lead to the instability of the doped Fe atom, increasing the PDS value in the corresponding pathways as was proposed in a previous investigation for ORR on a similar catalyst [8].

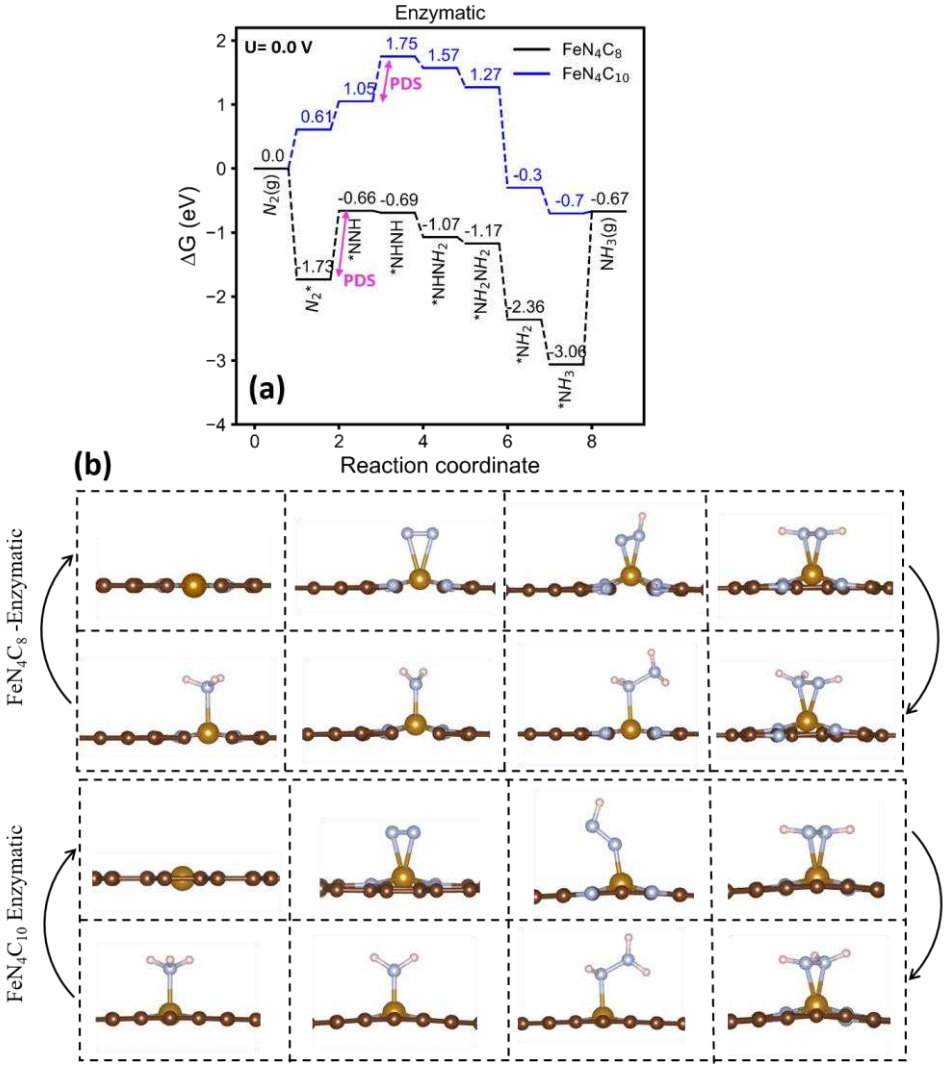

Figure S3. (a) The free energy diagram of the NRR through the enzymatic pathway on complexes A (black line) and B (blue line) at zero and applied potential. The PDS steps are shown in pink color. (b) The corresponding optimized adsorption configurations of the NRR intermediates on complexes A and B. Color code: brown, C; blue, N; orange, Fe; and white, H.

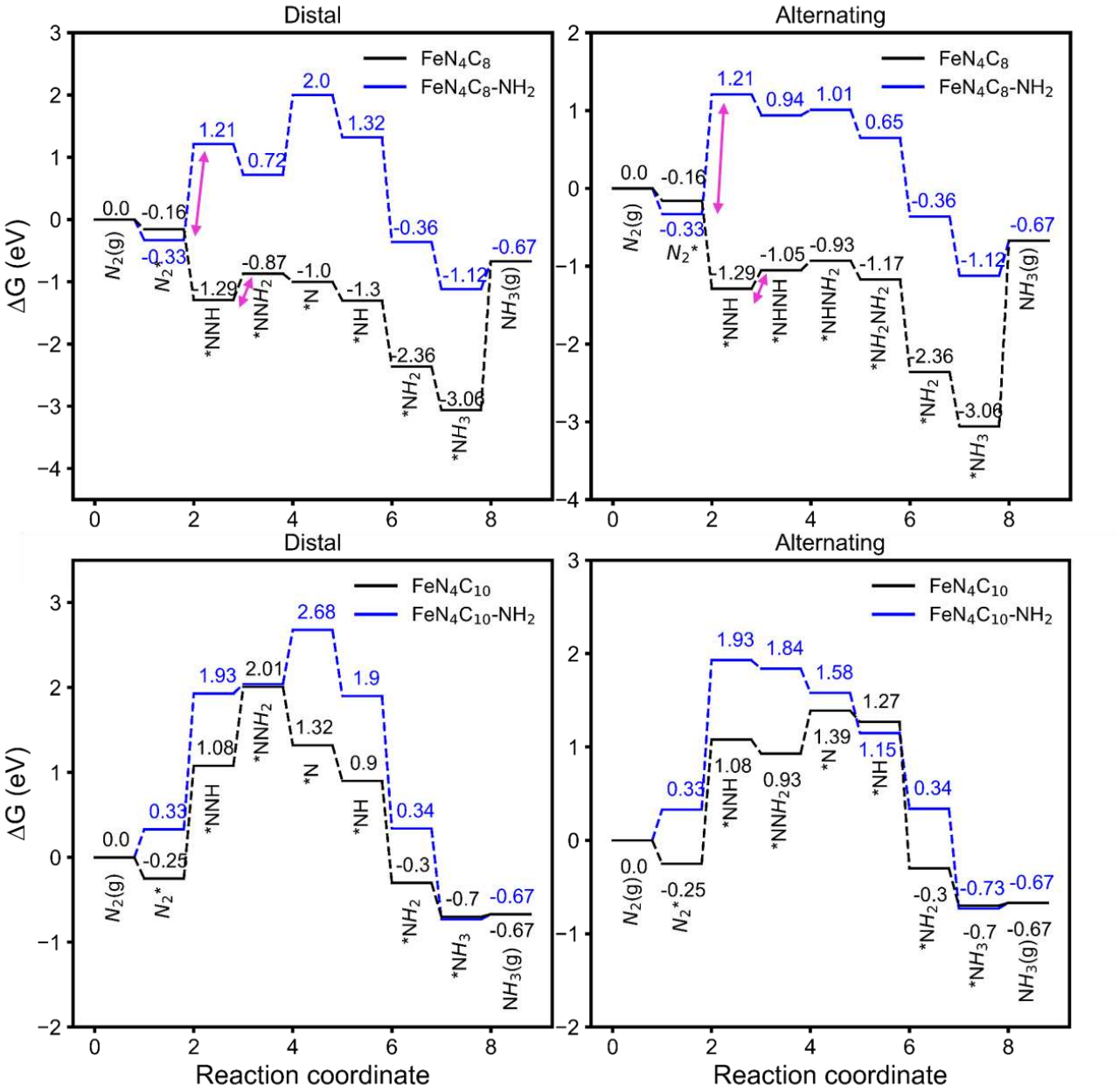

Figure S4. Comparison of the distal and alternating mechanisms on complexes A with C (top) with complexes B and D (bottom) at zero potential. The pink lines are the PDS steps.

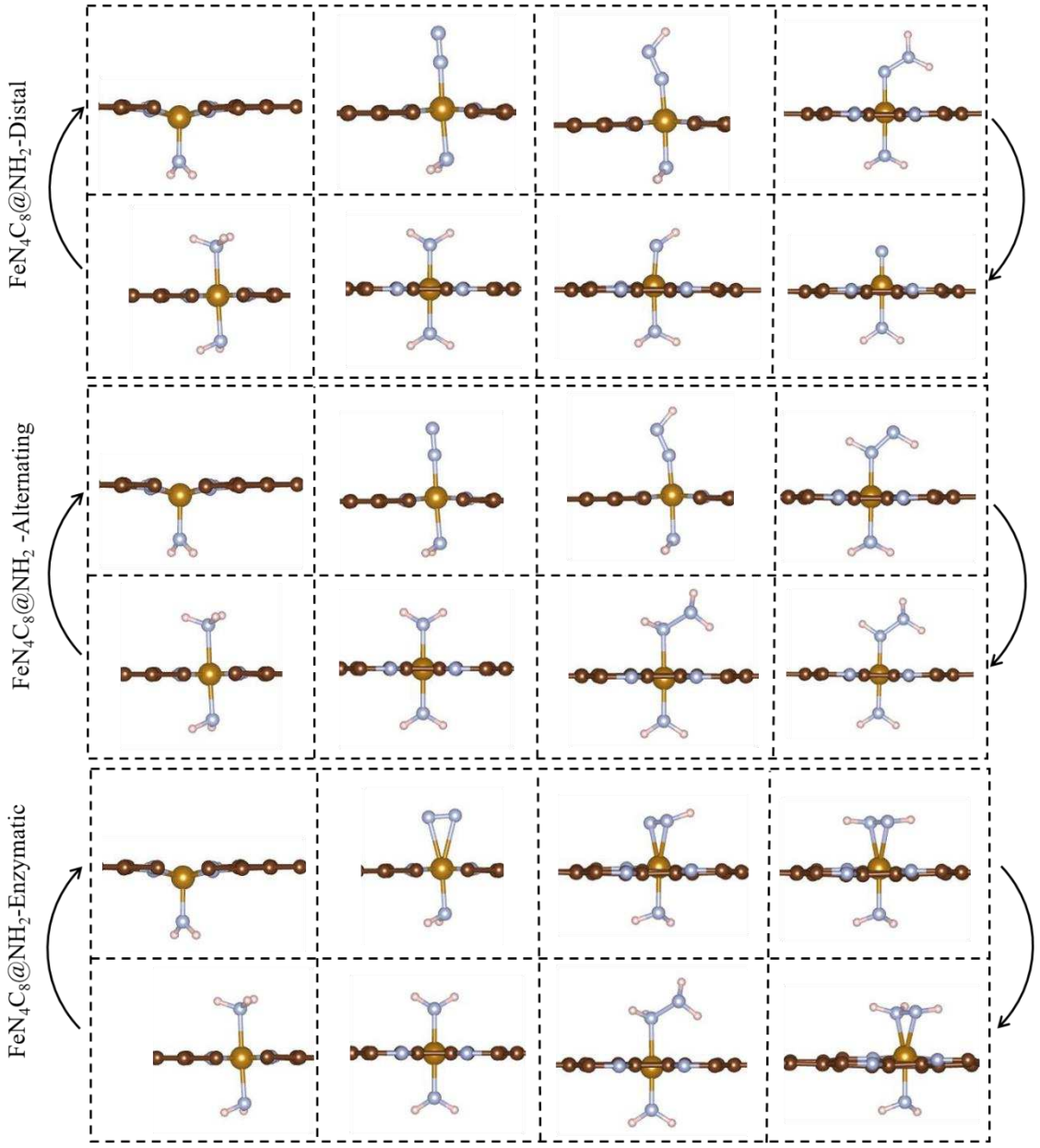

Figure S5. The optimized configurations of NRR intermediates on complex C through the distal, alternating, and enzymatic pathways. Color code: brown, C; blue, N; orange, Fe; and white, H.

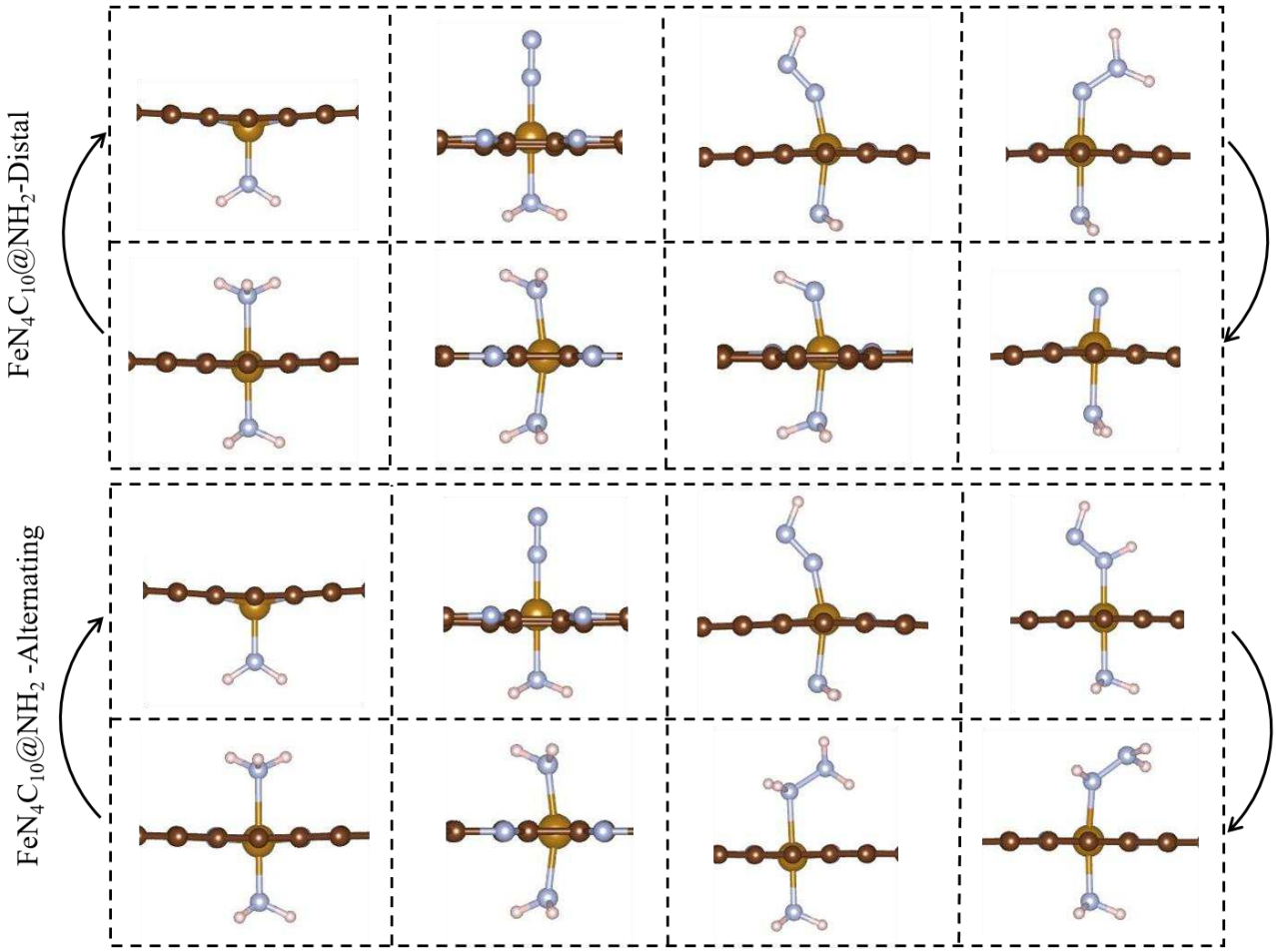

Figure S6. The optimized configurations of NRR intermediates on complex D through distal and alternating pathways. Color code: brown, C; blue, N; orange, Fe; and white, H.

Table S1. The computed average N-N bond length (d_{N-N}) of adsorbed $*N_2$ on complexes A, B, C, and D along with the corresponding adsorption energy (E_{ads}) of $*N_2$ and *H.

Complex	d_{N-N} (Å)		E_{ads}(eV)		
	$*N_2$ - endon	$*N_2$ - sideon	$*N_2$ - endon	$*N_2$ - sideon	*H
A	1.14	1.15	-0.61	-2.17	-2.06
C	1.14	1.14	-0.79	-0.06	0.05
B	1.14	1.16	-0.71	0.16	-0.03
D	1.14	1.12	-0.12	-0.18	0.69

Table S2. The computed average Fe-N bond length (d_{Fe-N}) of NRR intermediates, the adsorption energy (E_{ads}) of the Fe atom, the calculated NRR limiting potential (U_{lim}), and overpotential (**η**) on each complex in distal, alternating and enzymatic mechanism.

Complex	d_{Fe-N} (Å)- Distal							E_{ads-Fe} (eV)	U_L(V)	η (V)
	Pure	*NNH	$*NNH_2$	*N	*NH	$*NH_2$	$*NH_3$			
A	1.85	1.89	1.90	1.98	2.02	1.88	1.84	-4.52	-0.42	0.26
C	1.88	1.92	1.88	1.94	1.93	1.88	1.86	-	-1.54	1.38
B	1.88	1.93	1.92	1.93	1.90	1.90	1.90	-7.42	-1.33	1.17
D	1.91	1.94	1.91	1.90	1.94	1.93	1.90	-	-1.59	1.43

Complex	d_{Fe-N} (Å)- Alternating							E_{ads-Fe} (eV)	U_L(V)	η (V)
	Pure	*NNH	*NHNH	$*NHNH_2$	$*NH_2NH_2$	$*NH_2$	$*NH_3$			
A	1.85	1.88	1.85	1.85	1.84	1.88	1.84	-4.52	-0.24	0.08
C	1.88	1.92	1.88	1.92	1.91	1.88	1.86	-	-	1.38
B	1.88	1.93	1.90	1.90	1.89	1.90	1.90	-7.42	-1.33	1.17
D	1.91	1.94	1.90	1.92	1.90	1.93	1.90	-	-	1.43

Complex	d_{Fe-N} (Å)- Enzymatic							E_{ads-Fe} (eV)	U_L(V)	η (V)
	Pure	*NNH	*NHNH	$*NHNH_2$	$*NH_2NH_2$	$*NH_2$	$*NH_3$			
A	1.85	1.87	1.87	1.87	1.84	1.88	1.84	-4.52	-1.07	0.91
C	1.88	1.92	1.91	1.94	1.91	1.88	1.86	-	-1.82	1.66
B	1.88	1.93	1.90	1.92	1.89	1.90	1.90	-7.42	-0.70	0.54
D	1.91	-	-	-	-	-	-	-	-	-

Table S3. Quadrupole splitting energy (ΔE_{QS}) in $mm.s^{-1}$ for the catalysts containing ferrous moieties

Rows	Complex	ΔE_{QS} (S=0)	ΔE_{QS} (S=1)
1	Complex A	3.2	3.1
2	Complex B	3.3	3.2
3	NH@complex C	1.59	0.78
4	NH@complex D	1.24	0.58

Table S4. Quadrupole splitting energy (ΔE_{QS}) in $mm.s^{-1}$ for the catalysts containing ferric moieties

Rows	Complex	ΔE_{QS} (S=1/2)	ΔE_{QS} (S=3/2)	ΔE_{QS} (S=5/2)
1	Complex A@NH	1.09	1.59	0.85
2	Complex B@NH	1.77	1.40	1.21

References

1. Petrilli, H. M.; Blöchl, P. E.; Blaha, P.; Schwarz, K., Electric-Field-Gradient Calculations Using the Projector Augmented Wave Method. *Phys. Rev. B* **1998**, *57*, 14690.
2. Mineva, T.; Matanovic, I.; Atanassov, P.; Sougrati, M.-T.; Stievano, L.; Clémancey, M.; Kochem, A.; Latour, J.-M.; Jaouen, F., Understanding Active Sites in Pyrolyzed Fe–N–C Catalysts for Fuel Cell Cathodes by Bridging Density Functional Theory Calculations and 57fe Mossbauer Spectroscopy. *ACS Catal.* **2019**, *9*, 9359-9371.
3. Dufek, P.; Blaha, P.; Schwarz, K., Determination of the Nuclear Quadrupole Moment of 57 Fe. *Phys. Rev. Lett.* **1995**, *75*, 3545.
4. Nemykin, V. N.; Hadt, R. G., Influence of Hartree− Fock Exchange on the Calculated Mössbauer Isomer Shifts and Quadrupole Splittings in Ferrocene Derivatives Using Density Functional Theory. *Inorganic chemistry* **2006**, *45*, 8297-8307.
5. Shenoy, G. K.; Wagner, F., Mössbauer Isomer Shifts. **1978**.
6. Blaha, P. In *Calculations of Mössbauer Parameters in Solids by Dft Bandstructure Calculations*, Journal of Physics: Conference Series, IOP Publishing: 2010; p 012009.
7. Gallenkamp, C.; Kramm, U. I.; Proppe, J.; Krewald, V., Calibration of Computational Mössbauer Spectroscopy to Unravel Active Sites in Fenc Catalysts for the Oxygen Reduction Reaction. *International Journal of Quantum Chemistry* **2021**, *121*, e26394.
8. Jia, Q.; Ramaswamy, N.; Hafiz, H.; Tylus, U.; Strickland, K.; Wu, G.; Barbiellini, B.; Bansil, A.; Holby, E. F.; Zelenay, P., Experimental Observation of Redox-Induced Fe–N Switching Behavior as a Determinant Role for Oxygen Reduction Activity. *ACS Nano* **2015**, *9*, 12496-12505.